PERGAMON

International Journal of Heat and Mass Transfer 42 (1999) 1849–1862

International Journal of HEAT and MASS TRANSFER

Critical heat flux in a long, rectangular channel subjected to one-sided heating—II. Analysis of critical heat flux data

J.C. Sturgis, I. Mudawar*

Boiling and Two-Phase Flow Laboratory, School of Mechanical Engineering, Purdue University, West Lafayette, IN 47907, U.S.A.

Received 12 February 1998; in final form 3 August 1998

Abstract

A theoretical model to predict critical heat flux in long, rectangular channels is presented. The theoretical development is complemented by an extensive flow visualization analysis presented in Part I of this study. The observation of a periodic distribution of increasingly larger vapor patches along the surface just prior to CHF is idealized as a sinusoidal interface with amplitude and wavelength increasing in the flow direction. A separated flow model provides phase velocities and an average vapor thickness which are utilized by an instability analysis to predict the critical interfacial wavelength. An energy balance assumes the transfer of heat from the surface to the fluid occurs only at the troughs of the interface, called wetting fronts, and that the surface is insulated below the vapor patches. The lift-off of the most upstream wetting front, which occurs when the pressure difference serving to maintain interfacial contact with the surface is overcome by the vapor momentum emanating from the wetting front, is the trigger mechanism which precipitates CHF. The ratio of wetting front length to vapor wavelength obtained from the flow visualization represents a key contribution to the model. CHF predictions are accurate to within a mean absolute error of 10.0% for data obtained at near-saturated conditions for velocities of 0.25–10.0 m s^{-1}.

Nomenclature

A_f portion of flow area occupied by liquid
A_g portion of flow area occupied by vapor
A_l area of upstream wetting front
b ratio of liquid length to vapor wavelength, l/λ
c wave speed
c_i imaginary component of wave speed
c_p specific heat of liquid at constant pressure
c_r real component of wave speed
$C_{f,i}$ interfacial friction coefficient
$D_{h,f}$ hydraulic diameter of liquid phase
$D_{h,g}$ hydraulic diameter of vapor phase
f single-phase friction factor
g_e Earth's gravitational acceleration
g_n body force per unit mass normal to surface
G mass flux
h_{fg} latent heat of vaporization
H channel height
H_f liquid layer thickness
H_g vapor layer thickness
k wave number, $2\pi/\lambda$
k_{cr} critical wave number, $2\pi/\lambda_{cr}$
l length of wetting front used for modeling
l_j length of wetting front in heater segment j
l_{meas} liquid length measured between vapor patches
L length of heater
L_j length of heater segment j
$\dot{m}_b$ vapor mass flow rate in upstream wetting front normal to surface
n_j number of wetting fronts in heater segment j
P pressure
P_o pressure at outlet of heated section
$\overline{P_f - P_g}$ average interfacial pressure difference at wetting front
q'' heat flux
q''_j average wetting front heat flux for heater segment j
q''_m maximum nucleate boiling heat flux, CHF
q''_l heat flux concentrated at a wetting front
$q''_l(z^*)$ wetting front heat flux based on conditions at z^*

* Corresponding author. Tel.: 001 765 494 5705; fax: 001 765 494 0539; e-mail: mudawar@ecn.purdue.edu

0017–9310/98/$ - see front matter
PII: S0017–9310(98)00275–0

t time
T_o fluid temperature at outlet of heated section at CHF
U average inlet liquid velocity
$\bar{U}_f$ mean velocity of liquid phase
$\bar{U}_g$ mean velocity of vapor phase
$U_{g,n}$ vapor velocity in wetting front normal to surface
W channel width
x flow quality, $\rho_g \bar{U}_g \alpha / G$
y coordinate perpendicular to unperturbed interface
z streamwise coordinate, $z = 0$ at heater inlet
z^* extent of upstream continuous wetting front
z_0 distance from inlet to where $\bar{U}_f = \bar{U}_g$.

Greek symbols
α void fraction, δ / H
δ mean vapor layer thickness ($\delta = H_g$), vapor layer amplitude for CHF modeling
ΔT_{sub} local fluid subcooling
$\Delta T_{sub,o}$ fluid subcooling at outlet of heated section at CHF
ΔU phase velocity difference, $\bar{U}_g - \bar{U}_f$
η idealized sinusoidal perturbation of interface
η_0 maximum amplitude of sinusoidal perturbation, $\eta_0 = \delta$
λ vapor wavelength
λ_{cr} critical wavelength
λ_j vapor wavelength in heater segment j
λ_{meas} measured vapor patch length
μ viscosity
ρ density
ρ_f'' modified liquid density term, $\rho_f \coth(kH_f)$
ρ_g'' modified vapor density term, $\rho_g \coth(kH_g)$
σ surface tension
τ_i interfacial shear stress
$\tau_{w,f}$ shear stress associated with wall and liquid interactions
$\tau_{w,g}$ shear stress associated with wall and vapor interactions.

Subscripts
A accelerational
f saturated liquid
F frictional
g saturated vapor
j indicates heater segment, $j = 1, 2, 3, 4$
k indicates phase, f for liquid, g for vapor.

1. Introduction

For many applications it is vital to maintain heat loads below the critical heat flux limit in order to prevent catastrophic failure. For example, the integrity of electronic components requires heat loads to be maintained below CHF and in the case of a nuclear reactor accident, the consequences are more drastic when this limit is reached. Therefore, the ability to predict CHF for various flow boiling situations would be beneficial not only during the design phase of thermal devices, but during their operational lifetime as well.

Several models have been proposed by various researchers in an attempt to predict CHF and describe its mechanisms. Hughes and Olson [1] proposed a model based on a critical packing density of active sites on the surface. Each active nucleation site was associated with an area proportional to the diameter of the departing bubble. They postulated that CHF commences when the sum of these areas equals the total surface area, such that no additional sites can be activated.

Fiori and Bergles [2] postulated that CHF occurs when the liquid is no longer able to wet the surface. They indicated that the temperature of the wall below an attached vapor patch increases due to the insulating characteristic of the vapor. Once the patch detaches, bulk liquid rushes in and cools the wall. However, if the wall temperature has risen above the Leidenfrost point, the liquid will no longer be able to rewet the surface and CHF ensues.

The interfacial lift-off model, developed by Galloway and Mudawar [3], is based on the key observation from their flow visualization studies that a wavy vapor layer exists on the heated surface at fluxes just prior to critical heat flux. Liquid was observed to make contact with the surface at the wave troughs, called wetting fronts, and over a continuous upstream portion of the heater. They assumed that heat transfer to the fluid occurs only at these wetting locations while the regions underneath the peaks are dry. When the interface is lifted off the surface, wetting fronts are removed thereby eliminating paths for heat transfer, essentially insulating the surface with vapor and resulting in critical heat flux. Their model predicted their experimental critical heat flux values accurately but was limited to short heaters ($L \approx 12.7$ mm), low velocities ($U \leqslant 2$ m s^{-1}) and near-saturated conditions.

In addition to defining the CHF limit, a predictive tool should identify the parameters to which the critical heat flux is most sensitive, or insensitive. A model that is based on physical mechanisms and theoretical derivations often provides such characteristics whereas a correlation of experimental data may not be applicable to circumstances beyond the test conditions. It is with this mind-set that a mechanistic critical heat flux model is developed. Its construction draws on observations, physical mechanisms and theory with its evaluation based on the degree to which it predicts experimentally obtained data. The model which emerges is an extension of the interfacial lift-off model first developed by Galloway and Mudawar [3] and then modified by Gersey and Mudawar [4]. Inevitably, it is limited to certain conditions as a consequence of assumptions that are necessary to provide closure to the hydrodynamic and thermal aspects of the problem. However, the model does represent a mech-

anistically-based tool which accurately predicts the experimental CHF data.

2. Experimental apparatus

Experimental hardware and procedures are described in Part I of this study [5] which focuses on flow visualization of CHF. Only a brief overview of experimental aspects are presented here. Tests were conducted in a straight, rectangular channel having a 5.0×2.5-mm cross-section in which heat was applied to only one side, the shorter dimension, along a length of 101.6 mm. Critical heat fluxes obtained with FC-72 liquid at three outlet subcoolings ($\Delta T_{sub,o} = 3$, 16 and 29°C) over a broad range of velocity ($U = 0.25$–10 m s^{-1}) provided a basis with which to compare the model predictions. A constant outlet pressure, $P_o = 1.38$ bar, was maintained for all tests resulting in a constant outlet saturation temperature, $T_{sat,o} = 66.3$°C. A properly chosen inlet temperature led to the desired outlet fluid temperature, $T_o = 63.3$, 50.3 or 27.3°C, corresponding to the appropriate subcooling at the time of critical heat flux.

Flow visualization tests were conducted in a transparent channel using a Canon L1 8-mm video camera which was configured so that it could traverse the entire heated length. Flow boiling images were recorded for near-saturated ($\Delta T_{sub,o} = 3$°C) and subcooled ($\Delta T_{sub,o} = 29$°C) conditions for velocities of $U = 0.25$, 1, 2 and 4 m s^{-1}. Higher velocities were not attempted since vapor dimensions were approaching sizes too small to be measured reliably at $U = 4$ m s^{-1} and since the integrity of the transparent channel would be compromised at the higher wall temperatures associated with higher velocities. Measurements of length and height for numerous vapor patches permitted the characterization of vapor development along the heater. In some cases the flow visualization data were incomplete due to vapor patches being too small to be measured reliably.

The flow channel was oriented horizontally with gravity assumed to have negligible effects. Inertia and shear forces dominated the interaction between the liquid and vapor phases.

3. Analysis of critical heat flux data

The present analysis is based on the observations that at conditions just prior to CHF the vapor assumes a periodic, wave-like distribution along the heater surface. This observation is idealized by the wavy liquid–vapor interface depicted in Fig. 1. The idealization stems from the flow visualization studies presented in part I of this investigation [5] and is supported by the observations of Galloway and Mudawar [6] and Gersey and Mudawar [7]. Ideally, the vapor and liquid phases are separate with the waviness a result of instabilities between the two phases. It is assumed that heat transfer occurs only at discrete locations where liquid contacts the surface and that the heater surface beneath a wave is adiabatic during the passage of vapor. CHF is postulated to occur when the interface detaches from the surface eliminating the wetting fronts available for the transfer of heat. This lifting off of the interface occurs when the momentum of vapor generated at a wetting front overcomes the pressure force holding the interface in contact with the surface. This is the observed trigger mechanism for CHF which provides a criterion for calculating the lift-off heat flux [3].

The theoretical development of the model therefore incorporates four major components: a separated flow model; an instability analysis; a heater energy balance; and a lift-off criterion. Additionally, flow visualization plays a key role by providing support for some of the empirically determined liquid–vapor interface characteristics. Each of these components, and the manner in which they interrelate, are discussed.

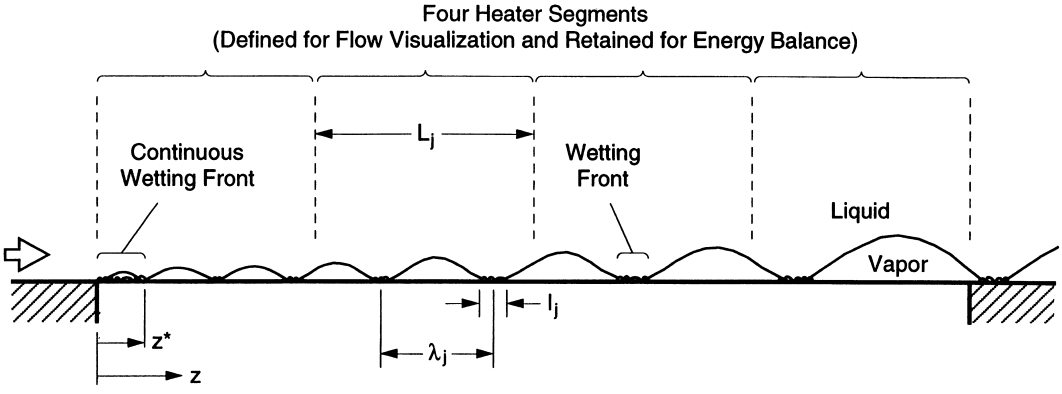

Fig. 1. Idealized wavy liquid–vapor interface showing vapor and liquid definitions and heater segments.

3.1. Separated flow model

Analysis of two-phase flow is often treated in an idealized fashion by assuming that the vapor and liquid phases are completely separate with a distinguishable interface. For the case of flow in a rectangular channel heated on one wall, the vapor phase is adjacent to the heated wall and has a mean thickness δ that increases in the streamwise direction. Though the vapor does not actually exist with a smooth interface having a monotonically increasing thickness, this does represent an effective starting point for developing a CHF model since it provides information about average vapor thickness and mean velocities for the vapor and liquid phases. The difference in phase velocities is responsible for the instabilities that create the waviness which has been observed. Therefore, the main contribution of the separated flow model to the CHF model is the determination of liquid phase velocity, $\bar{U}_f$, vapor phase velocity, $\bar{U}_g$, and average vapor layer thickness, δ. The separated flow model yields each of these parameters as a function of streamwise coordinate z.

Each phase is treated as a separate fluid characterized by its own velocity and momentum terms and bound by the channel walls as well as the other phase. Consequently, conservation of mass, momentum and energy are applied to the vapor phase, as well as the entire two-phase flow, to arrive at expressions for the phase velocities and vapor layer thickness. Assumptions employed in the separated flow model are: (1) the two-phase flow is one-dimensional; (2) change of phase occurs only at the heated wall with no condensation at the interface; (3) wall flux is uniform and constant along the heated wall; (4) vapor layer has steady, uniform thickness at any location z; (5) vapor layer begins at leading edge of heater, $z = 0$; (6) liquid subcooling remains constant along the flow; and (7) vapor remains at its saturation temperature.

Assumptions (2) and (6) lead to the conclusion that the entire wall flux is used to increase the temperature of a mass of liquid from its inlet temperature to its saturation temperature and then to convert this mass to saturated vapor, adding mass to the vapor phase. Therefore, continuity applied to a vapor control volume results in an expression for average vapor velocity, $\bar{U}_g$,

$$\bar{U}_g = \frac{q''z}{\rho_g \delta [c_p \Delta T_{sub} + h_{fg}]}. \tag{1}$$

Mass conservation applied to the entire cross-section leads to the average liquid velocity, $\bar{U}_f$,

$$\bar{U}_f = \frac{UH}{H-\delta} - \frac{q''z}{\rho_f (H-\delta)[c_p \Delta T_{sub} + h_{fg}]}. \tag{2}$$

Similarly, conservation of momentum may be applied to the vapor control volume and the channel control volume separately, with Fig. 2 indicating the relevant force and momentum terms for each. Vapor generated at the wall has been assumed to have no initial streamwise velocity and, as such, does not contribute streamwise momentum to the control volume. The resulting expressions for streamwise vapor pressure gradient, dP_g/dz, and channel pressure gradient, dP/dz, are given, respectively, by

$$-\frac{dP_g}{dz} = \frac{1}{\alpha}\frac{d}{dz}\left(\frac{x^2 G^2}{\alpha \rho_g}\right) + \frac{1}{\alpha HW}[\tau_{w,g}(W + 2\alpha H) + \tau_i W] \tag{3}$$

and

$$-\frac{dP}{dz} = \left(-\frac{dP}{dz}\right)_A + \left(-\frac{dP}{dz}\right)_F \tag{4}$$

where

$$\left(-\frac{dP}{dz}\right)_A = \frac{d}{dz}\left(\frac{x^2 G^2}{\alpha \rho_g} + \frac{(1-x)^2 G^2}{(1-\alpha)\rho_f}\right) \tag{5}$$

$$\left(-\frac{dP}{dz}\right)_F = \tau_{w,g}\left[\frac{1}{H} + \frac{2}{W}\alpha\right] + \tau_{w,f}\left[\frac{1}{H} + \frac{2}{W}(1-\alpha)\right]. \tag{6}$$

Equation (4) indicates that the overall pressure in the channel is comprised of two components—accelerational and frictional. The accelerational effect is due to net vapor generation—as mass is converted to less dense vapor, flow area for the liquid is restricted requiring an increase in its velocity to preserve continuity. Frictional losses account for interaction of both phases with the channel walls. Had the channel not been oriented horizontally, gravity would have also contributed a term to the streamwise pressure gradient.

The vapor and liquid layers are in mechanical equilibrium and, hence, pressure is constant throughout both phases at a given cross-section. Therefore, the two gradients are equal at all streamwise locations, providing closure to the separated flow model. The vapor layer thickness, δ, for a particular location z is chosen such that the vapor and channel pressure gradients are equal; this requires iteration of δ.

The shear stress terms in equations (3) and (6) may be expressed by

$$\tau_{w,k} = \frac{1}{2}\rho_k \bar{U}_k^2 \left(\frac{f_k}{4}\right) \tag{7}$$

where k indicates phase, either vapor, g, or liquid, f. For the case of turbulent flow in a smooth pipe, the friction factor may be approximated by

$$f_k = 0.184\left[\frac{\rho_k \bar{U}_k D_{h,k}}{\mu_k}\right]^{-1/5} \tag{8}$$

where the hydraulic diameter for each phase is

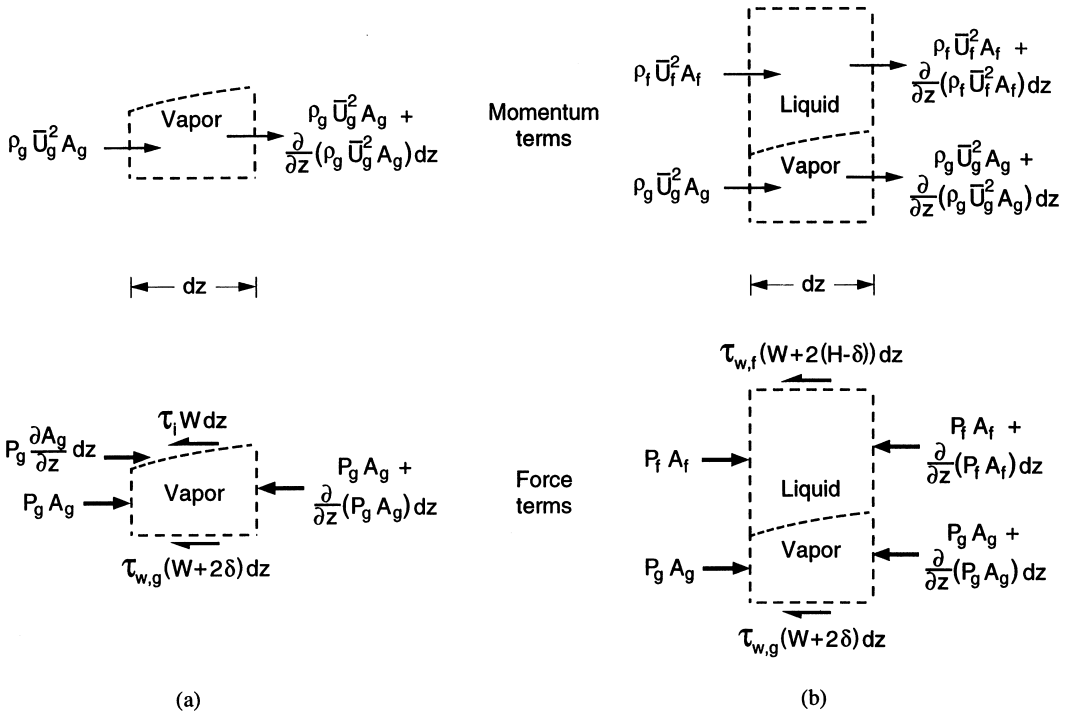

Fig. 2. Momentum and force terms pertaining to (a) vapor and (b) channel control volume.

$$D_{h,g} = \frac{2W\delta}{W+\delta} \tag{9}$$

$$D_{h,f} = \frac{2W(H-\delta)}{W+H-\delta} \tag{10}$$

This allows for the estimation of shear between the vapor and channel walls, $\tau_{w,g}$, and between the liquid and channel walls, $\tau_{w,f}$. The interfacial shear between the two phases may be evaluated in a similar manner by

$$\tau_i = \frac{1}{2}\rho_g(\bar{U}_g - \bar{U}_f)^2 C_{f,i} \tag{11}$$

The interfacial friction coefficient, $C_{f,i}$, may be approximated by several correlations, but Galloway and Mudawar [3] found good agreement with their data by using a constant value of $C_{f,i} = 0.5$.

This analysis yields a profile for each of $\bar{U}_f$, $\bar{U}_g$ and δ as a function of z, determined through an iterative method. Calculations show that the velocity of the vapor phase increases rapidly due to the addition of the low density vapor, while the liquid phase velocity increases more slowly. As a result, the phase velocity difference, $\Delta U = \bar{U}_g - \bar{U}_f$, increases along the heater. It is this velocity difference that is responsible for the instability of the interface and is an important input to the instability analysis.

3.2. Instability analysis

Flow visualization studies reveal that the vapor assumes a wavy distribution along the heater surface which suggests an analysis of its stability. For this case, the situation has been idealized as the classical case of two fluids moving relative to each other between two infinite parallel walls. Disturbances can lead to an unstable interface and the goal is to find the wavelength of the interface which is neutrally stable; that is, on the verge of becoming unstable. A wave under this condition would be most susceptible to the momentum flux of vapor emanating from the wetting fronts.

Therefore, classical instability theory [8] is utilized assuming a sinusoidal interface with small curvature, depicted in Fig. 3. Using the phase velocity difference and vapor layer thickness obtained from the separated flow model along with known property values, the critical wavelength, λ_{cr}, may be calculated. This derivation assumes irrotational, inviscid and incompressible flow with small interfacial curvature.

The velocity field, with mean and perturbation components, may be determined by solving the Laplace equation for the liquid and vapor velocity potentials. With these known, Bernoulli's equation may be employed to determine the pressure field. It is the pressure difference

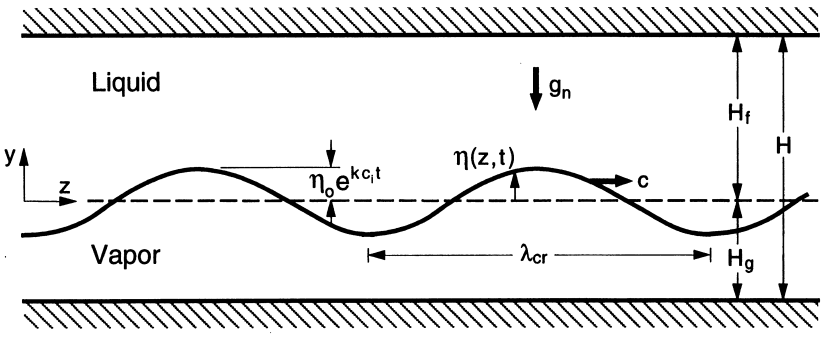

Fig. 3. Wavy interfacial boundary between liquid and vapor phases in a rectangular channel.

across the interface that is of interest since it gives rise to the curvature and instability.

The interface is assumed to take the form of a simple harmonic wave expressed as

$$\eta(z,t) = \eta_0 \, e^{ik(z-ct)} \tag{12}$$

where only the real part represents the actual interface and the imaginary part will provide a criterion for interfacial stability. η_0 represents the wave amplitude ($\eta_0 = \delta$), k the wave number ($k = 2\pi/\lambda$) and the c wave speed. For a small perturbation of this interface, the instability analysis leads to a pressure difference expressed by

$$P_f - P_g = -\left[\rho_f''(c-\bar{U}_f)^2 + \rho_g''(\bar{U}_g - c)^2 + (\rho_f - \rho_g)\frac{g_n}{k}\right] k\eta_0 \, e^{ik(z-ct)} \tag{13}$$

where the modified density terms are given by $\rho_f'' = \rho_f \coth(kH_f)$ and $\rho_g'' = \rho_g \coth(kH_g)$. Alternately, the pressure difference across a mildly curved interface may be approximated as the product of surface tension and curvature, resulting in

$$P_f - P_g \approx \sigma\frac{\partial^2\eta}{\partial z^2} = -\sigma\eta_0 k^2 \, e^{ik(z-ct)}. \tag{14}$$

Equating these two expressions for pressure difference yields a quadratic expression for wave speed, c,

$$\rho_f''(c-\bar{U}_f)^2 + \rho_g''(\bar{U}_g - c)^2 + (\rho_f - \rho_g)\frac{g_n}{k} - \sigma k = 0 \tag{15}$$

which, upon solving, yields

$$c = \frac{\rho_f''\bar{U}_f + \rho_g''\bar{U}_g}{\rho_f'' + \rho_g''} \pm \sqrt{\frac{\sigma k}{\rho_f'' + \rho_g''} - \frac{\rho_f''\rho_g''(\bar{U}_g - \bar{U}_f)^2}{(\rho_f'' + \rho_g'')^2} - \frac{(\rho_f - \rho_g)}{(\rho_f'' + \rho_g'')}\frac{g_n}{k}}. \tag{16}$$

Since an imaginary component of wave speed suggests an unstable interface, the terms under the radical reveal the effects of the different forces. The first term accounts for surface tension which always provides a stabilizing force. The second term is the inertial force which is always destabilizing. Finally, the gravitational force may be stabilizing or destabilizing depending on the orientation of the gravity vector with respect to the vapor layer.

The condition for stability may be identified by rewriting the interface relation, equation (12), allowing for the possibility of a complex wave speed, $c = c_r + ic_i$.

$$\eta = \eta_0 \, e^{ik(z-ct)} = \eta_0 \, e^{c_i kt} \, e^{ik(z-c_r t)} \tag{17}$$

If the wave speed is purely a real number then the interface is sinusoidal. If it is complex, then for $c_i < 0$, the interface is stable, diminishing in amplitude, while for $c_i > 0$ it is unstable. Neutral stability occurs, and the critical wavelength is defined, when $c_i = 0$. The real and imaginary components of the wave speed are, respectively,

$$c_r = \frac{\rho_f''\bar{U}_f + \rho_g''\bar{U}_g}{\rho_f'' + \rho_g''} \tag{18}$$

$$c_i = \sqrt{\frac{\rho_f''\rho_g''(\bar{U}_g - \bar{U}_f)^2}{(\rho_f'' + \rho_g'')^2} + \frac{(\rho_f - \rho_g)}{(\rho_f'' + \rho_g'')}\frac{g_n}{k} - \frac{\sigma k}{\rho_f'' + \rho_g''}}. \tag{19}$$

Therefore, setting equation (19) equal to zero and solving for k yields the desired expression for critical wavelength, λ_{cr}.

$$k_{cr} = \frac{2\pi}{\lambda_{cr}} = \frac{\rho_f''\rho_g''(\bar{U}_g - \bar{U}_f)^2}{2\sigma(\rho_f'' + \rho_g'')} + \sqrt{\left[\frac{\rho_f''\rho_g''(\bar{U}_g - \bar{U}_f)^2}{2\sigma(\rho_f'' + \rho_g'')}\right]^2 + \frac{(\rho_f - \rho_g)g_n}{\sigma}}. \tag{20}$$

Calculation of λ_{cr} with this expression requires iteration since λ_{cr} is contained in the modified density terms, ρ_f'' and ρ_g''. The critical wavelength is determined from knowledge of fluid properties (ρ_f, ρ_g, σ) and flow parameters ($\bar{U}_f, \bar{U}_g, H_f = H - \delta, H_g = \delta$) which are determined from the separated flow analysis.

As discussed previously, the pressure difference across the interface is incorporated into the CHF model through the lift-off criterion. Figure 4 shows the dependence of critical wavelength, λ_{cr}, and average pressure difference,

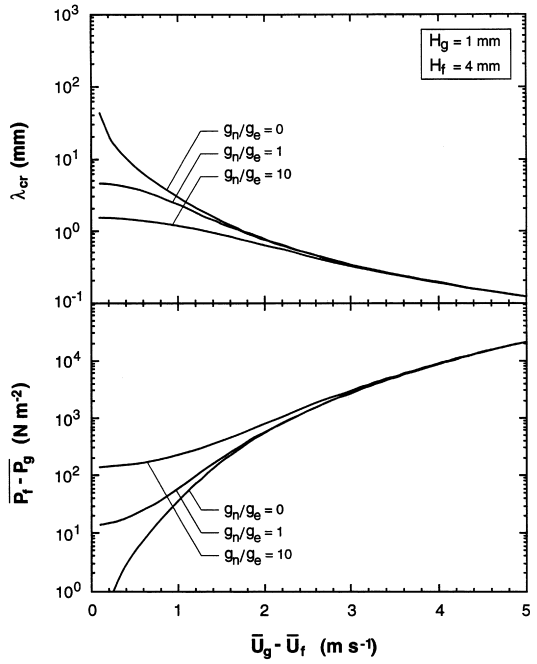

Fig. 4. Effect of phase velocity difference and body force on critical wavelength and average pressure difference (based on λ_{cr}) for flow in a rectangular channel in which the average vapor layer thickness is 1 mm.

$\overline{P_f - P_g}$, on interfacial velocity difference, $\Delta U = \bar{U}_g - \bar{U}_f$, for an average vapor layer thickness of 1.0 mm. For this plot, pressure difference has been averaged over a wetting front that is one-fourth the critical wavelength. The critical wavelength decreases with increasing velocity difference whereas the pressure difference increases. For low velocity differences, λ_{cr} decreases for larger magnitudes of the normal body force while for $\Delta U \geqslant 2.5$ m s^{-1}, the normal force has no influence on either λ_{cr} or $\overline{P_f - P_g}$, indicating instability is dominated by inertial effects. Similar trends exist for average vapor layer thicknesses of 2.0 and 4.0 mm.

Assuming no body forces, the critical wavelength may be expressed as

$$\lambda_{cr} = \frac{2\pi\sigma(\rho_f'' + \rho_g'')}{\rho_f''\rho_g''(\bar{U}_g - \bar{U}_f)^2}. \tag{21}$$

The instability analysis also yields the theoretical length of the upstream wetting front, z^*, where it is defined as

$$z^* = z_0 + \lambda_{cr}(z^*). \tag{22}$$

Measured from the leading edge, z_0 is the location on the heater where the vapor phase velocity just exceeds the liquid phase velocity. Beyond this location, the vapor velocity continues to increase faster than the liquid and instability between the phases is more likely to take place. The vapor then assumes the wavy formation one critical wavelength beyond this point where the continuous wetting front ends. Since λ_{cr} is evaluated at z^*, which itself is an unknown, iteration must also be employed in determining z^*.

Table 1 show the theoretical vapor characteristics based on the separated flow model and instability analysis for near-saturated conditions. The experimental critical heat flux has been used in the separated flow model to determine the phase velocities, vapour thickness and $z_o \cdot \lambda_{cr}$ is shown to decrease with increasing velocity indicating more wetting fronts on the heater for higher velocities. The trend of decreasing vapor length with increasing velocity was shown by the video images in Part I of this study [5].

Although this instability analysis has been idealized, it is valuable in that it provides information regarding a theoretical wavelength characterizing the interaction of the vapor and liquid phases. In yielding values for the critical wavelength and upstream liquid wetting region, it provides a theoretical component to the CHF model.

3.3. Energy balance

The energy balance is constructed with reference to the wavy vapor layer depicted in Fig. 1. The liquid makes contact with the heater over a distance z^* at the leading edge and at discrete wetting fronts. These wetting fronts are crucial to maintaining effective cooling of the surface and are the focus of the energy balance. Knowing the length and number of these wetting fronts, one can construct an instantaneous energy balance.

Flow visualization results indicate that the wavelength increases along the flow direction thereby spacing the wetting fronts farther apart. Liquid wetting length also increases along the flow direction but remains a constant fraction of the local wavelength. The energy balance should account for these variations. In the present investigation, the heater length was divided into four segments (each approximately 25 mm long) for flow visualization purposes and this division is retained for the construction of the energy balance. This segmentation enables the energy balance to account for the continuous stretching of the wavelength by using different average vapor lengths for each segment; essentially discretizing the heated length. Likewise, the length and number of wetting fronts are accounted for in each segment.

The energy balance expresses that the sum of energy dissipated at all wetting fronts, including the continuous upstream wetting front, is equal to the energy dissipated by a flux acting over the entire heated surface. This flux is taken as the critical heat flux, q_m'', for the heater. Therefore, the energy balance yields the expression

$$q_m'' = \frac{1}{L - z^*}[q_1'' l_1 n_1 + q_2'' l_2 n_2 + q_3'' l_3 n_3 + q_4'' l_4 n_4]. \tag{23}$$

Table 1
Theoretical vapor characteristics determined from separated flow model and instability analysis for near-saturated conditions ($\Delta T_{sub,o} = 3°C$) in rectangular channel based on measured CHF

U (m s^{-1})	CHF (W cm^{-2})	z_0 (mm)	$\lambda_{cr}(z^*)$ (mm)	z^* (mm)	$\delta(z^*)$ (mm)	$\bar{U}_g - \bar{U}_f$ at z^* (m s^{-1})	$\delta(L)$ (mm)
0.25	25.0	0.17	6.56	6.74	1.10	0.60	4.14
0.5	25.0	0.34	4.35	4.68	0.59	0.70	3.48
1	28.2	0.61	2.84	3.44	0.34	0.83	2.86
1.5	30.5	0.89	2.26	3.15	0.25	0.91	2.50
2	32.1	1.20	1.95	3.15	0.22	0.98	2.25
3	34.6	1.88	1.64	3.52	0.19	1.08	1.91
4	36.8	2.62	1.49	4.10	0.19	1.16	1.69
5	36.5	3.68	1.44	5.11	0.19	1.20	1.48
6	37.8	4.64	1.38	6.04	0.20	1.25	1.36
7	42.3	5.05	1.31	6.35	0.20	1.32	1.32
8	46.9	5.38	1.24	6.61	0.20	1.38	1.29
9	52.9	5.43	1.15	6.58	0.20	1.46	1.29
10	62.8	4.89	1.05	5.93	0.20	1.55	1.35

The z^* term accounts for the continuous upstream wetting front where a flux equal to the critical heat flux is assumed. l_j is the average wetting front length and n_j the number of wetting fronts, each for the jth segment. The flux associated with a wetting front is denoted by q''_j, where j takes the values 1, 2, 3 or 4 depending on which segment is being referenced.

The number of wetting fronts is given by

$$n_j = \begin{cases} \dfrac{L_1 - z^*}{\lambda_1} & \text{for } j = 1 \\ \dfrac{L_j}{\lambda_j} & \text{for } j = 2, 3, 4 \end{cases} \tag{24}$$

where L_j is the length of the heater segment and λ_j the average wavelength characterizing the jth segment. Intuitively, n_j should be an integer value but is allowed to assume fractional values. Dividing the segment length, L_j, by the wavelength, λ_j, and truncating the remainder does not reflect the number of wetting fronts which exist in the heater segment on a time-averaged basis, nor does truncating the remainder and adding one to account for the wetting front at the beginning of the segment. Figure 5 shows three possible positions of a vapor wave relative to a heater segment. Over time, this segment will see one, one and a partial, or two wetting fronts available for heat transfer with the average being between 1 and 2. Requiring n_j to be an integer leads to a low or a high estimate whereas allowing n_j to be real will lead to a value between the extremes. Therefore, allowing the number of wetting fronts to take on fractional values is an attempt to extend an instantaneous energy balance to account for average conditions. The consequences of doing so are not significant. Rather, this provides a smooth, monotonic function leading to only one solution for the iterative scheme.

The length of a wetting front, l_j, is based on flow visualization measurements. l_j is referenced to the local wavelength by the ratio b, which is defined by

$$b = \frac{\text{wetting front length}}{\text{vapor wavelength}} = \frac{l_j}{\lambda_j}. \tag{25}$$

Given the wavelength and b, the wetting front length can be calculated. As discussed in Part I of this study, the value of b is relatively constant along the heater and for all velocities of the same subcooling. Therefore, one value of b applies to a particular subcooling condition. This is an important conclusion from the flow visualization

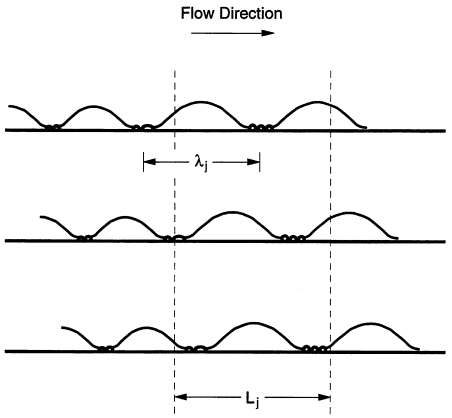

Fig. 5. Vapor wave of wavelength λ_j on heater surface such that one, one and a half or two wetting fronts exist in heater segment of length L_j.

study that differs from the work of Gersey and Mudawar [7]. They postulated that the wetting length remains constant along the flow direction whereas in the present study it is found to increase in proportion to the increasing vapor wavelength. This has important implications for the energy balance.

A consequence of the wetting front length increasing proportionately with vapor wavelength is that the product ($l_j n_j$) in the energy balance eliminates the need to determine a predictive relation for wavelength. Mathematically, this is shown for the first segment by

$$l_1 n_1 = (b\lambda_1)\frac{L_1 - z^*}{\lambda_1} = b(L_1 - z^*) \tag{26a}$$

and for the downstream segments ($j = 2, 3, 4$) by

$$l_j n_j = (b\lambda_j)\frac{L_j}{\lambda_j} = bL_j. \tag{26b}$$

This has beneficial consequences for the model development. Since the ratio of wetting front length to vapor wavelength is constant along a heater and with increasing velocity, which has been demonstrated by the flow visualization measurements, the modeling effort may be extended to velocities beyond which flow visualization was performed. The relations given in equation (26) are introduced into the energy balance in the next section along with an approximation for the flux concentrated at a wetting front, q''_l.

3.4. Lift-off criterion

The remaining elements of the energy balance equation (23) are the fluxes concentrated at the wetting fronts, expressions for which are obtained by invoking the lift-off criterion. CHF is postulated to occur when the momentum flux of vapor emanating from the surface overcomes the pressure force tending to maintain interfacial contact with surface [6]. The interface then detaches from the surface eliminating a wetting front which represents a path for heat transfer to the liquid. The fluxes in the remaining wetting fronts must then increase to accommodate this loss with the eventual outcome being the lift-off of the interface at these locations as well. This lift-off of the interface and elimination of a sufficient number of wetting fronts trigger the critical heat flux condition.

An expression for this lift-off flux may be determined by equating the average pressure force acting to maintain interfacial contact with the vapor momentum tending to push the interface away, illustrated in Fig. 6. For a mildly curved interface, this pressure difference, $P_f - P_g$, is proportional to the curvature and given by equation (14). This represents the pressure difference across a wavy interface with the value being positive at the wetting fronts. The force which opposes the vapor momentum is approximated as the average pressure force existing over

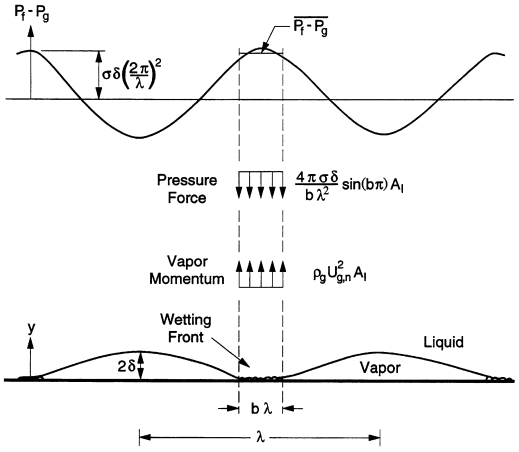

Fig. 6. Average pressure difference and vapor momentum at wetting front used to determine lift-off heat flux.

the length of the wetting front. Therefore, integrating equation (14) over the length $l = b\lambda$ centered at the wetting front, as indicated in Fig. 6, yields an analytical expression for average pressure difference.

$$\overline{P_f - P_g} = \frac{4\pi\sigma\delta}{b\lambda^2}\sin(b\pi). \tag{27}$$

The vapor momentum flux, $\rho_g U_{g,n}^2$, is determined from an energy balance applied to the wetting front region. The flux concentrated at a wetting front, q''_l, raises the temperature of a mass of liquid to its saturation temperature and the converts it to saturated vapor. This is expressed as

$$q''_l A_l = (c_p \Delta T_{sub} + h_{fg})\dot{m}_b = (c_p \Delta T_{sub} + h_{fg})\rho_g U_{g,n} A_l \tag{28}$$

where A_l is the area associated with the wetting front and $U_{g,n}$ the vapor velocity normal to the surface. Solving for $U_{g,n}$ and equating the vapor momentum emanating from the heater surface with the average pressure force, lead to the desired expression for the local lift-off heat flux.

$$q''_l = \rho_g (c_p \Delta T_{sub} + h_{fg})\left[\frac{\overline{P_f - P_g}}{\rho_g}\right]^{1/2} \tag{29}$$

where $\overline{P_f - P_g}$ is given by equation (27).

These expressions provide a means for estimating lift-off fluxes given the characteristics—λ, δ, b—of the vapor layer. Since there are insufficient vapor measurements to describe the wavy interface for all conditions, a means of establishing a lift-off flux based on other criteria is sought. Galloway and Mudawary postulated that the lift-off of the most upstream wetting front is the trigger mechanism for CHF. That is, once the conditions are sufficient to detach the first wetting front, all others quickly follow. Therefore, the wetting front fluxes indicated in equation (23) are approximated as the flux sufficient to detach a wetting front located at z^*. This provides a straight-

forward manner for calculating the wetting front fluxes in the absence of data on vapor wavelengths and thicknesses at higher velocities.

The use of λ_{cr}, and not $2\lambda_{cr}$ as used by Galloway and Mudawar [3] and Gersey and Mudawar [4], in determining lift-off flux at z^* is based on newly obtained vapor measurements from the side-view visualization study presented in Part I [5]. The measurements of Galloway and Mudawar were also made from a side perspective but were obtained with a short heater ($L = 12.7$ mm) at lower velocities ($U \leqslant 1$ m s^{-1}). Hence, the validity of their $2\lambda_{cr}$ assumption may be limited to these extreme conditions which are associated with weaker interfacial pressure forces and a tendency of the most upstream wetting front to more easily skip attachment, leading to their observed $2\lambda_{cr}$ wavelength. Gersey and Mudawar found that the first few wavelengths measured on each of their three heaters were approximately λ_{cr}. They noted that since their view was normal to the surface, some of the measured waves could have been in the process of lifting from the surface. Therefore, they adopted the use of $2\lambda_{cr}$ in the calculation of lift-off flux. In regards to the present investigation, initial vapor lengths measured over the upstream segment of the heater translate into wavelengths near λ_{cr} for an idealized wavy interface. The relation between λ_{meas} and λ may be expressed in the following manner by using $\lambda = \bar{\lambda}_{meas} + \bar{l}_{meas}$ (from Part I) and the definition of b (equation (25)).

$$\lambda(z) = \lambda_{meas}(z) + \bar{l}_{meas} = \lambda_{meas}(z) + b\lambda(z) \tag{30}$$

$$\lambda(z) = \frac{\lambda_{meas}(z)}{1-b}. \tag{31}$$

In this manner, the ratio $\lambda(z)/\lambda_{cr}$ is plotted in Fig. 7 based on vapor lengths measured along the heater for near-saturated conditions at $U = 1$ m s^{-1}. The initial data points ($7 < z < 12$ mm) are clustered around unity indicating that the first waves created on the heater just prior to CHF have a wavelength close to the critical wavelength; in this case, $\lambda = \lambda_{cr} = 2.84$ mm. Therefore, the lift-off flux is calculated assuming the interface is characterized by the critical wavelength, λ_{cr}, average vapor height at z^*, $\delta(z^*)$, and liquid-to-vapor ratio, b.

Now all of the terms of the energy balance have been established. Substituting the relations given in equation (26) for the products $(l_j n_j)$ into the energy balance equation (23) and noting that the wetting front fluxes are given by

$$q''_j = q''_l(z^*) \tag{32}$$

yields a simplified expression for the estimation of CHF, q''_m.

$$q''_m = bq''_l(z^*) \tag{33}$$

This expression states that the flux concentrated at the wetting fronts is $1/b$ times the critical heat flux since the latter is taken as an average value acting over the entire heated surface. This expression clearly shows that the model estimation for CHF is a combination of theoretical arguments, yielding $q''_l(z^*)$, and physical observations, yielding b.

3.5. Flow visualization

The major contributions of the visualization study are support for modeling the vapor as a wavy profile and quantification of vapor and liquid dimensions. The video

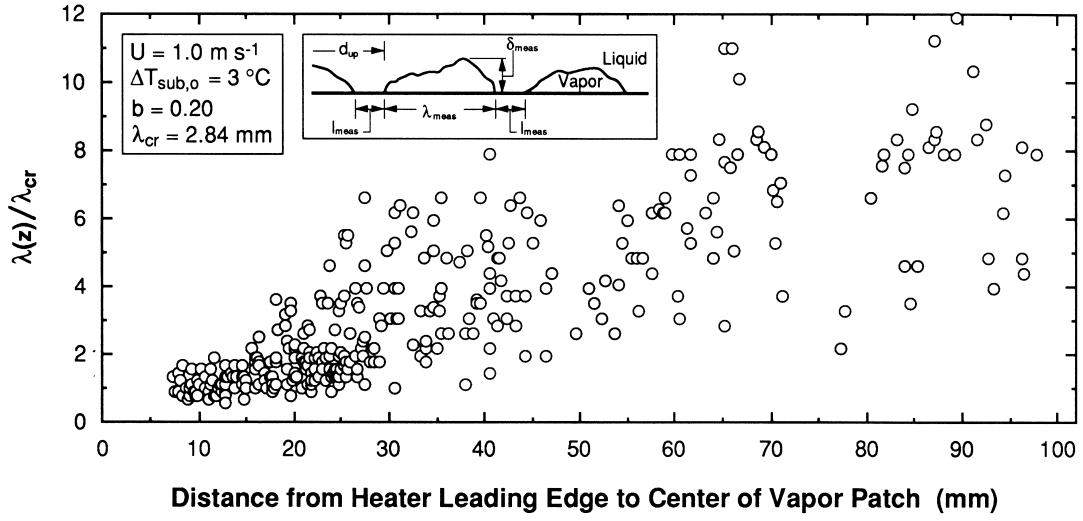

Fig. 7. Ratio of vapor wavelength to critical wavelength versus distance to center of vapor patch at CHF for near-saturated conditions and $U = 1$ m s^{-1}.

sequences allowed for numerous vapor patches to be observed with common vapor shapes noted and their percentage of occurrence determined. By so doing, it was noted that an overhanging vapor formation did not occur significantly enough in the channel to deem it a significant contributor to critical heat flux. Some models have proposed that CHF occurs when the overhanging vapor isolates a portion of the heated surface from the cooler bulk [9]. Once the trapped sublayer of liquid is converted to vapor, the large overhanging patch restricts liquid from rushing in to rewet the surface, resulting in an increase in wall temperature. For continued passages of overhanging vapor, the wall temperature continues to increase eventually culminating in critical heat flux. While the overhanging vapor formation was observed, the prominent formation is the generic vapor patch that has a maximum thickness near its center, typical of a portion of a wave. It is important to emphasize, however, that occurrence of overhanging vapor formation became statistically significant at highly subcooled conditions for which the Lee and Mudawar model [9] was developed. The wave-like formation was observed in the present study in all segments of the heater often separated by short lengths of liquid-surface contact. This provided excellent validation for the underlying model assumption of an idealized wavy vapor layer (Fig. 1) existing on the surface just prior to CHF.

Flow visualization also served to quantify the vapor and liquid dimensions. Measurements concluded that the length of the wetting front, which directly affects the energy balance, increases in the flow direction but remains approximately the same fraction of the local wavelength. This observation highlights a difference with the models presented by Galloway and Mudawar [3] and Gersey and Mudawar [4] which assume a constant wetting front length along the heater. These models use a liquid-to-vapor length ratio of $b = 0.25$ based largely on the flow visualization study of Galloway and Mudawar [6] conducted with near-saturated FC-87 liquid and a short heater. For present investigation with a long heater, this ratio is fairly constant along the channel and among velocities with the same subcooling, having the values $b = 0.2$ for near-saturated ($\Delta T_{\mathrm{sub,o}} = 3^{\circ}\mathrm{C}$) conditions and $b = 0.3$ for highly subcooled ($\Delta T_{\mathrm{sub,o}} = 29^{\circ}\mathrm{C}$) flow. This increase indicates that cooler bulk temperatures are better able to break up the vapor and allow liquid to contact the surface. The CHF model is able to reflect this trend by incorporating this ratio.

3.6. CHF model construction

As described above, the model incorporates four major components in the estimation of critical heat flux. The solution is not an explicit expression but rather a procedure requiring numerical integration along the heater and iterations at several levels. An overview of the procedure is given in Fig. 8 and described below.

After setting subcooling and flow velocity, the solution process is initiated by guessing a value for the critical heat flux. This value is used in the separated flow model to determine the phase velocities, $\bar{U}_f$ and $\bar{U}_g$, and vapor layer thickness, δ, for every z location along the heater. The solution for these values requires iteration at each location until the vapor pressure gradient, $\mathrm{d}P_g/\mathrm{d}z$, is equal to the channel pressure gradient, $\mathrm{d}P/\mathrm{d}z$.

The output of the separated flow model is then used in the instability analysis to determine the critical wavelength, λ_{cr}, and the extent of the upstream wetting front, z^*. This requires another series of iterations.

Once the critical wavelength and upstream wetting length are known, the energy balance can be established. However, since the wetting length remains proportional to the vapor wavelength, the energy balance is not an explicit function of either l_j or λ_j, but rather their ratio.

Next, the average interfacial pressure difference at z^* is calculated and then used in evaluating the lift-off flux at z^*. This flux, to be used in the energy balance, is a function of pressure difference, subcooling, vapor thickness and critical wavelength. Flow visualization contributes the liquid-to-vapor length ratio.

The energy balance then yields a value for the critical heat flux. This value is compared with the estimated value which initiated the process. If they are sufficiently close in value, then the critical heat flux for the given velocity has been predicted. If not, a new critical heat estimate (based on bisection method) is used to re-initiate the process which continues until the iteration converges on a value.

3.7. CHF model predictions

The CHF model was applied for near-saturated conditions over the entire range of velocity for which data have been obtained. Constant properties were assumed because of the small changes in temperature and pressure. Variations in subcooling along the flow have very little influence on the phase velocities and vapor layer thickness as determined by the separated flow model. For this reason, subcooling was fixed at the inlet value for the near-saturated case. Theoretically, this means that the local bulk temperature remains constant; not exactly true but an acceptable approximation for this case. Flow visualization aided in the construction of the model in that it quantified the liquid-to-vapor length ratio which was observed to be approximately 0.2. This value held for all segments along the heater indicating that as the wavelength grew so did the wetting length in a proportionate amount.

The model estimates for critical heat flux are shown by the solid curve in Fig. 9, along with the experimentally obtained data, for near-saturated conditions. Con-

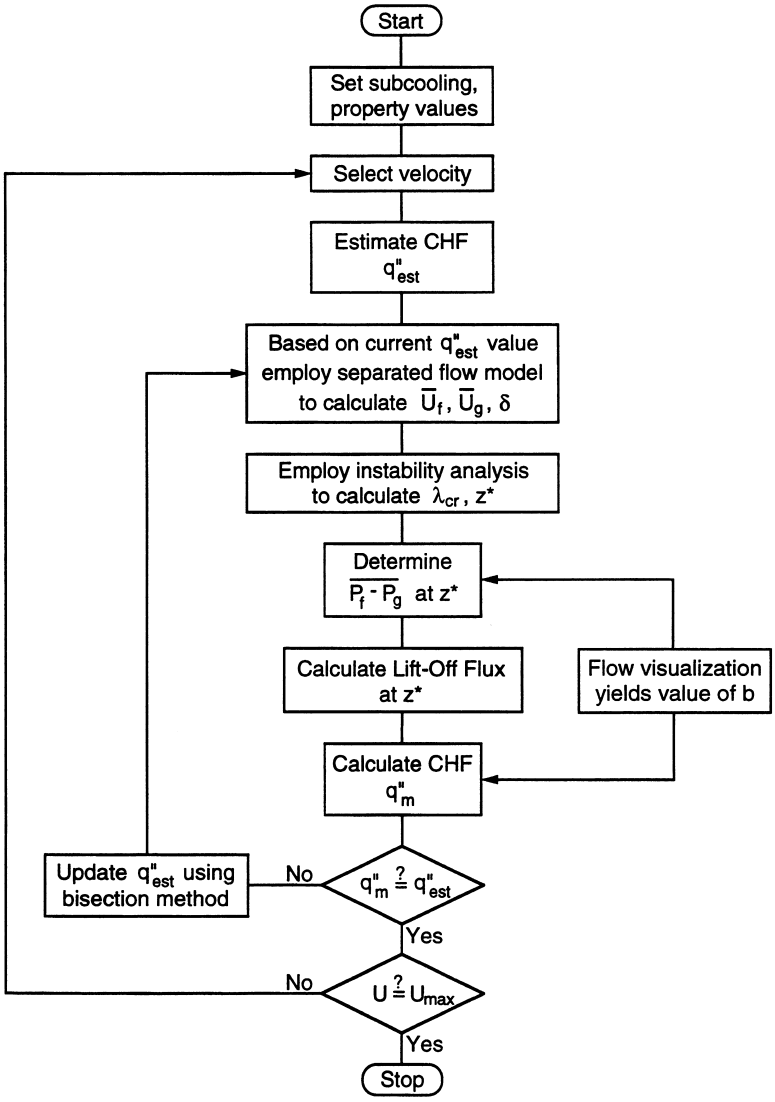

Fig. 8. Solution procedure for CHF model.

sidering the entire range of velocity, the model predicts values to within a mean absolute error of 10.0%. The maximum error for velocities greater than 0.25 m s^{-1} is 17.0% corresponding to $U = 6$ m s^{-1}. This represents a good degree of accuracy considering the assumptions employed throughout the derivation. The trend of the prediction is also intuitive, showing CHF increasing with velocity.

Attempts to extend this model to subcooled flow ($\Delta T_{sub,o} = 29°C$) using the subcooled flow visualization data were not as successful. The mean absolute error of predictions was 24.8% relative to the experimental values. Though the model yielded increasing CHF with increasing velocity, the slope did not reflect the behavior of the data. Interfacial condensation was the most troublesome aspect for modeling subcooled conditions. The separated flow model, which estimates the amount of vapor production based on heat input, does not account for vapor condensation which would cause an increase in temperature of the surrounding liquid. This is one reason why the model accurately predicts CHF for near-saturated conditions, in which case negligible condensation is a reasonable approximation, but does not handle subcooled conditions very well. The model needs to address this by considering factors which affect the condensation rate, such as phase velocity difference, phase temperature difference and vapor surface area. Flow visualization images from part I reveal strong con-

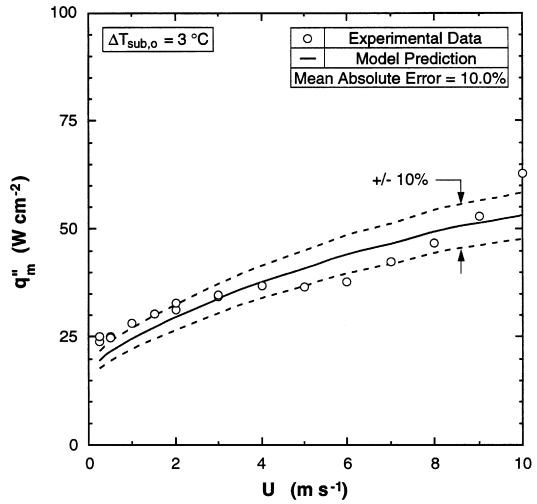

Fig. 9. CHF data and model predictions for near-saturated conditions.

trast between the vapor–liquid interfaces in near-saturated and subcooled flows. This condensation issue, which is beyond the scope of the present study, should be carefully assessed in future modeling of subcooled flow boiling CHF.

The CHF model may be applied to similar near-saturated situations with knowledge of liquid/vapor properties, channel geometry and flow conditions. In predicting CHF for these new situations, the present values for liquid-to-vapor length ratio ($b = 0.2$) should be employed first. However, measurements of vapor and liquid dimensions for a few select velocities in the situation of interest would help fine tune the model, especially in relation to the magnitude of b.

4. Conclusions

Extending the work of Galloway and Mudawar [3], a critical heat flux model for flow boiling in a long, rectangular channel was presented. It incorporates qualitative and quantitative results obtained through a flow visualization investigation presented in Part I of this study. Key findings can be summarized as follows:

(1) Conditions just prior to CHF can be described and accurately idealized by a wavy vapor layer which grows in thickness and wavelength along the heated wall. Cooling of the wall is possible only through the troughs, wetting fronts, of the vapor wave.
(2) Prior to CHF, liquid access to the wall is possible due to an interfacial pressure force tending to maintain contact of the liquid–vapor interface with the wall as the wavy interface propagates downstream. CHF is triggered by lift off of the upstream wetting front when the momentum of vapor normal to the wall ultimately exceeds the interfacial pressure force.
(3) A CHF model based on this interfacial lift-off criterion was developed. The model is a combination of theoretical arguments, which are used to predict the lift-off heat flux, and physical observations, which provided an estimate for the ratio of wetting front length to vapor wavelength.
(4) The CHF model includes subtle improvements over the model first proposed by Galloway and Mudawar [3], including an analytical expression for the lift-off heat flux, a more accurate estimate for the ratio of wetting front length to vapor wavelength, and a better description of the lift off of the upstream wetting front. Additionally, unlike the earlier model, the present CHF model is validated for a long heater and over a very broad range of velocity.
(5) The present model predicts near-saturated CHF data in long channels to within a mean absolute error of 10.0%. The predicted trends are both intuitively reasonable and numerically accurate, lending credibility to the assumptions employed.
(6) Interfacial condensation undermines the assumptions of the separated flow model incorporated in the CHF model for highly subcooled conditions. Hence, the present model is not recommended for these conditions. Interfacial condensation should therefore be carefully evaluated in any future modeling of highly subcooled flow boiling CHF.

Acknowledgments

The authors are grateful for the support of the Office of Basic Energy Sciences of the U.S. Department of Energy (Grant No. DE-FG02-93ER14394.A003). Financial support for the first author was provided through the Air Force Palace Knight Program.

References

[1] T.G. Hughes, D.R. Olson, Critical heat fluxes for curved surfaces during subcooled flow boiling, U.S. National Heat Transfer Conference, vol. 3, San Francisco, CA, 1975, pp. 122–130.
[2] M.P. Fiori, A.E. Bergles, Model of critical heat flux in subcooled flow boiling, Heat Transfer 1970: Proceedings from the Fourth International Heat Transfer Conference, Paper B6.3, Paris, 1970.
[3] J.E. Galloway, I. Mudawar, CHF mechanism in flow boiling from a short heated wall—II. Theoretical CHF model, International Journal of Heat and Mass Transfer 36 (1998) 2527–2540.
[4] C.O. Gersey, I. Mudawar, Effects of heater length and orien-

tation on the trigger mechanism for near-saturated flow boiling critical heat flux—II. CHF model, International Journal of Heat and Mass Transfer 38 (1995) 643–654.

[5] J.C. Sturgis, I. Mudawar, Critical heat flux in a long, rectangular channel subjected to one-sided heating—I: flow visualization, International Journal of Heat and Mass Transfer 42 (1999) 1835–1847.

[6] J.E. Galloway, I. Mudawar, CHF mechanism in flow boiling from a short heated wall—I. Examination of near-wall conditions with the aid of photomicrography and high-speed video imaging, International Journal of Heat and Mass Transfer 36 (1993) 2511–2526.

[7] C.O. Gersey, I. Mudawar, Effects of heater length and orientation on the trigger mechanism for near-saturated flow boiling critical heat flux—I. Photographic study and statistical characterization of the near-wall interfacial features, International Journal of Heat and Mass Transfer 38 (1995) 629–641.

[8] L.M. Milne-Thomson, Theoretical Hydrodynamics, 4th ed., MacMillan, New York, 1960.

[9] C.H. Lee, I. Mudawar, A mechanistic critical heat flux model for subcooled flow boiling based on local bulk flow conditions, International Journal of Multiphase Flow 14 (1988) 711–728.